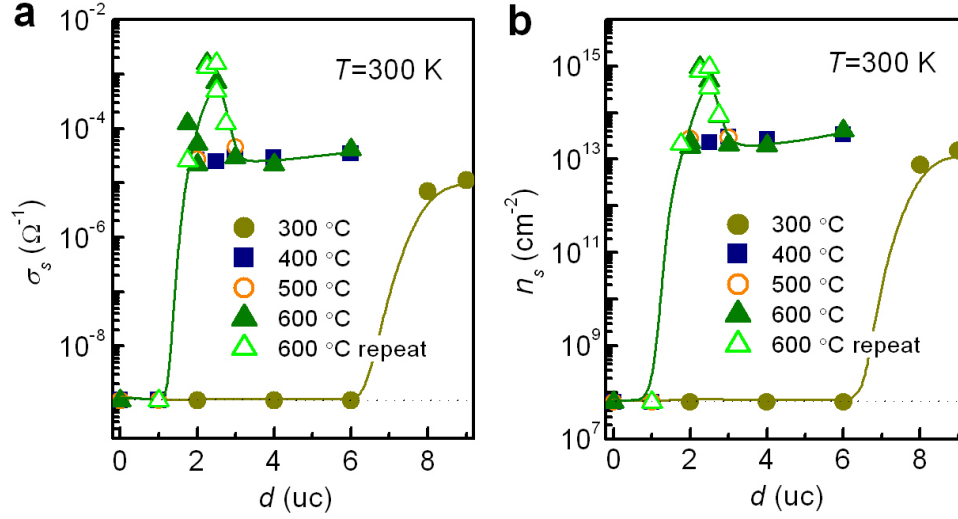


Supplementary Figure S1. Layer-by-layer epitaxial growth of γ - Al_2O_3 films on (001)-oriented SrTiO_3 (STO) with TiO_2 -termination. **a**, The RHEED intensity oscillations for the film growth at different deposition temperatures, T_s . Remarkably, the epitaxial growth of γ - Al_2O_3 /STO spinel/perovskite heterostructures is observed even at room temperature (20 °C). At $T_s < 100$ °C, a gradual decrease in the RHEED peak intensity with increasing film thickness is observed. Moreover, the RHEED pattern (shown in **b**) may disappear when the film thickness is above 50 oscillations (10 nm), probably due to the evolution of amorphous films with increasing film thickness. In contrast, at $T_s > 100$ °C, both RHEED intensity oscillations and sharp RHEED patterns can keep up to a film thickness of 100 oscillations (about 20 nm), suggesting a persistent layer-by-layer two-dimensional film growth mode. In each case, streaky RHEED pattern along with clear Kikuchi lines can be observed, indicating the high crystalline quality of the epitaxial film. Note that, at $T_s \leq 400$ °C, there is a huge transient increase of the RHEED intensity once the film deposition is started, which is followed by a corresponding decrease in the RHEED intensity when the deposition is interrupted. This behaviour has

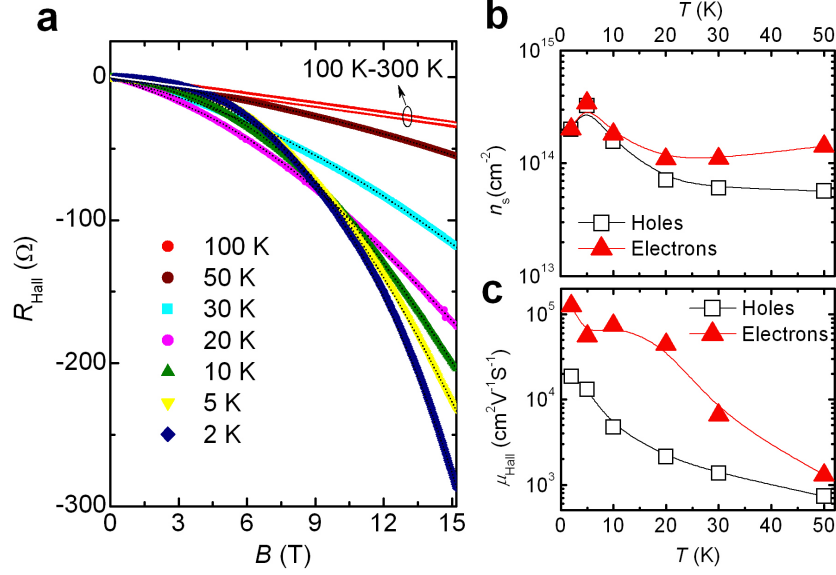
been ascribed to the changes in the step density on the surface or the reconstruction of the substrate surface [41, 42]. However, at $T_s > 400$ °C, such phenomena disappear. We suggest that it may be related to the charging induced surface reconstruction at low temperatures ($T_s \leq 400$ °C) where the high-temperature *p*-type conduction in bulk STO single crystal (due to unintentional acceptors) is negligible. All the films grown at $T_s > 200$ °C show a regular terrace surface, as show in **c** for a 10 $\mu\text{m} \times 10 \mu\text{m}$ atomic force microscopy image. The regular terraces show steps of 0.4 nm in height following that of the STO substrate. The epitaxial growth of the film with $\gamma\text{-Al}_2\text{O}_3$ (400)<001>//STO (200)<001> is also confirmed by HRTEM measurements and the image simulation as illustrated in **d**.



Supplementary Figure S2. Thickness dependent interfacial conduction for $\gamma\text{-Al}_2\text{O}_3/\text{STO}$

heterostructures grown at different temperatures. a and b, Sheet conductance, σ_s , and carrier density, n_s , respectively, measured at 300 K. The conductivity of each $\gamma\text{-Al}_2\text{O}_3/\text{STO}$ heterostructure is investigated. Under the conditions used in this manuscript, samples deposited at $T_s < 300$ °C are all insulating with the sheet resistance higher than $10^9 \Omega/\square$ (the measurement limit). While, heterostructures grown at $T_s \geq 300$ °C become conductive when the film thickness is above a critical thickness, as shown in **a**. For all conductive samples, Hall effect measurements show a negative Hall resistance (see also Fig. S3), indicating an n-type dominant conduction. When increasing T_s , a sharp decrease in the critical thickness for the occurrence of interface conduction is observed (from approximately 6 uc at $T_s = 300$ °C to 2 uc at $T_s = 400$ °C). For all $\gamma\text{-Al}_2\text{O}_3/\text{STO}$ heterostructures grown at $T_s < 600$ °C, the highest obtained electron mobility is below $3000 \text{ cm}^2\text{V}^{-1}\text{s}^{-1}$ at 2 K. While a strong increase in the electron mobility is observed at $T_s = 600$ °C, where we also observe the convex shape of the curve for sheet conductance versus film thickness. Further increasing T_s deteriorates both conductivity and mobility. Therefore, the data above 600 °C are not shown. It should be noted that the

sharp change in conductivity with respect to film thickness in addition to the extremely high electron mobilities exceeding $100,000 \text{ cm}^2\text{V}^{-1}\text{s}^{-1}$ at 2 K can be reproduced in our $\gamma\text{-Al}_2\text{O}_3/\text{SrTiO}_3$ heterostructures grown at 600 °C, as also illustrated in the figure.



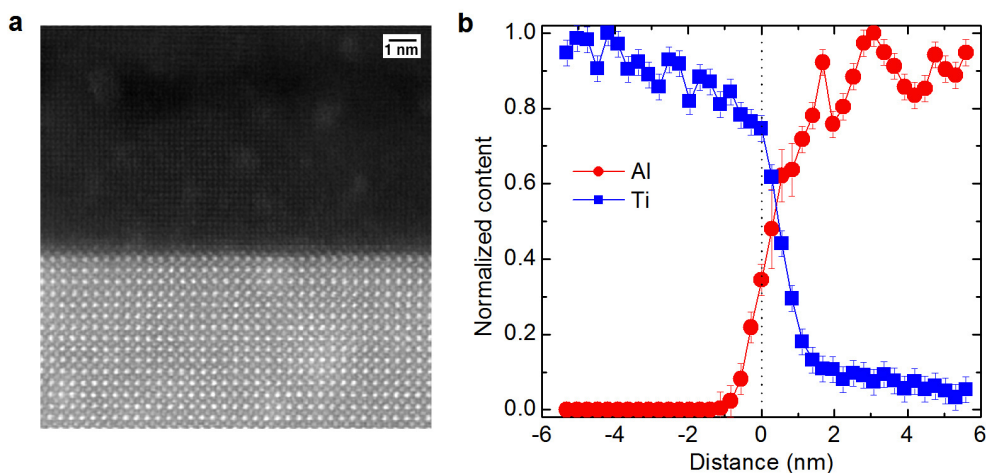
Supplementary Figure S3. The Hall resistance of the γ -Al₂O₃/STO interface at $d=2.5$ uc. **a**, Hall resistance (R_{Hall}) versus magnetic field at different temperatures. A normal Hall effect, i.e. a linear relation in the Hall resistance with respect to magnetic fields is observed at temperatures from 300 K to 100 K (white line in **a**). However, a strong non-linearity in the Hall resistance versus magnetic fields is observed upon cooling below 50 K. Such nonlinear Hall effect probably arises from a multichannel conduction involving different electronic bands and/or spatially separated parallel conducting channels, which can be explained by a two-band model [27, 43]. In this model, the Hall-resistance and the longitudinal resistance at zero magnetic field can be expressed as:

$$\rho_{xy} = \frac{\sigma_1^2 R_1 + \sigma_2^2 R_2 + \sigma_1^2 \sigma_2^2 R_1 R_2 (R_1 + R_2) B^2}{(\sigma_1 + \sigma_2)^2 + \sigma_1^2 \sigma_2^2 (R_1 + R_2) B^2} B$$

$$\rho_{xx}(0T) = \frac{1}{\sigma_1 + \sigma_2}$$

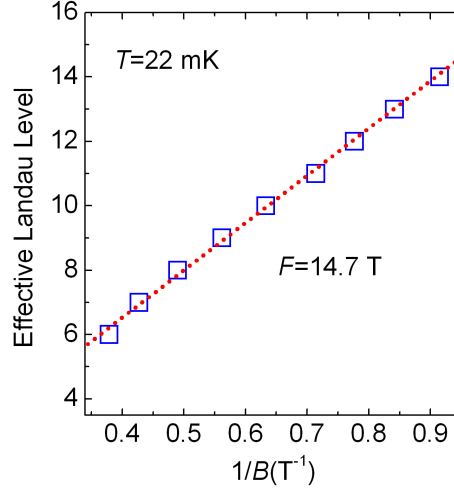
Where, $\sigma_{1,2} = |n_{1,2} e \mu_{1,2}|$, and $R_{1,2} = (n_{1,2} e)^{-1}$.

As shown in **a** (black dot lines), the Hall resistance below 50 K can be well fitted by the above two-band model with the constraint of zero field resistance. It should be noted that no fit to the data could be obtained if both bands are of electron-type as reported for the perovskite-type heterointerfaces [27, 43]. This indicates that hole conduction presents or becomes apparent at our spinel/perovskite γ - Al_2O_3 /STO heterointerfaces. The hole conduction could result from the substitution of Ti by Al due to cation intermixing, or the possible deficiency of Ti due to its extended outward diffusion as determined by STEM-EELS (Fig. S4). The fitted data for carrier density and mobility are shown in **b** and **c**. The most remarkable feature for the outcome of the fitting is that it gives an electron mobility of $1.3 \times 10^5 \text{ cm}^2 \text{V}^{-1} \text{s}^{-1}$ at 2 K, which is almost the value ($1.4 \times 10^5 \text{ cm}^2 \text{V}^{-1} \text{s}^{-1}$) deduced from the Hall measurements at low magnetic fields as shown in the main text. Since the Hall effect is always linear in our samples with the highest mobility less than $10,000 \text{ cm}^2 \text{V}^{-1} \text{s}^{-1}$, in order to compare different samples, the charge carrier density and Hall mobility deduced from the Hall measurements at low magnetic fields are adopted in the main text (also for the sake of comparing the data over the whole temperature range of 2-300 K). It should be noted that the Hall measurements always give the information on the total/net charge carriers. The fact that the hole conduction becomes visible in our 2.5 μc sample (at low temperatures), may be just because the mobility of electrons becomes much higher than that of holes. This is also supported by the fact that the nonlinear Hall effect becomes more apparent in samples with more higher electron mobilities.



Supplementary Figure S4. Cation profile across the γ -Al₂O₃/STO interface by STEM-EELS. a, A large-area STEM image of the Al₂O₃/STO. **b**, The normalized spatial distribution of Ti and Al across the interface by integrating the EELS line scans from the Ti-L and Al-L edges, respectively. The main feature of this chemical profile lies in the rather limited inward diffusion of Al within 1.0 nm into STO. In contrast, Ti shows extended outward diffusion into the γ -Al₂O₃ film with diffusion length larger than 5.5 nm away from the interface. The asymmetric diffusion may result from the intrinsic structure difference between spinel and perovskite. For spinel oxides, there are plenty of cation vacancies inside the structure, which makes it rather easier for cation exchanges within the oxygen sublattices. The barrier for the cation diffusion in spinel oxide can be as low as 0.6 eV [44, 45]. In contrast, the cation migration barrier is much larger in STO, which is normally higher than 3.0 eV [46]. Under such a situation, we cannot rule out the possibility that the TEM sample preparation process may aggravate the cation intermixing observed here. However, the existence of Ti outward diffusion in the as-deposited samples is also confirmed by XPS measurements. Moreover, both XPS and EELS results indicate that the Ti⁴⁺ is the dominant component for the outdiffused Ti. Additionally, the asymmetric cation diffusion leads to Ti vacancies on the STO side, which can extend 4 nm deep into STO as shown in **b**.

Such cation vacancies are expected to compensate the oxygen-vacancies-dominated interface conduction. This may explain why there is a drop in the interface conduction when the film thickness is higher than approximately 2.5 μm as shown in Fig. 2d and e in the text.



Supplementary Figure S5. Two-dimensional electron density at the $\gamma\text{-Al}_2\text{O}_3/\text{STO}$ interface and

the mean free path of electrons. SdH oscillations represent a direct measurement of the area of the

Fermi surface. The cross-sectional area, A , of the Fermi surface normal to the magnetic field can be

deduced by the Onsager relation: $F = \frac{\hbar}{2\pi e} A$, where F is the SdH frequency. Assuming a circular

section of the Fermi surface, the carrier density can be estimated by: $n_{2D} = g_v g_s e F / h$, where g_v and

g_s are the valley and spin degeneracy, respectively. Fig. S5 is the index plots of $1/B_n$ versus the

effective Landau level index for the $d=2.25$ μm sample. B_n is obtained from the position of the

maximum of ΔR_{xx} between 1 T and 3 T at $T=22$ mK (see Fig. 4 in the main text). The best-fit straight

line (red dots) gives a Fermi cross-section corresponding to $F=14.7$ T. By taking a single valley

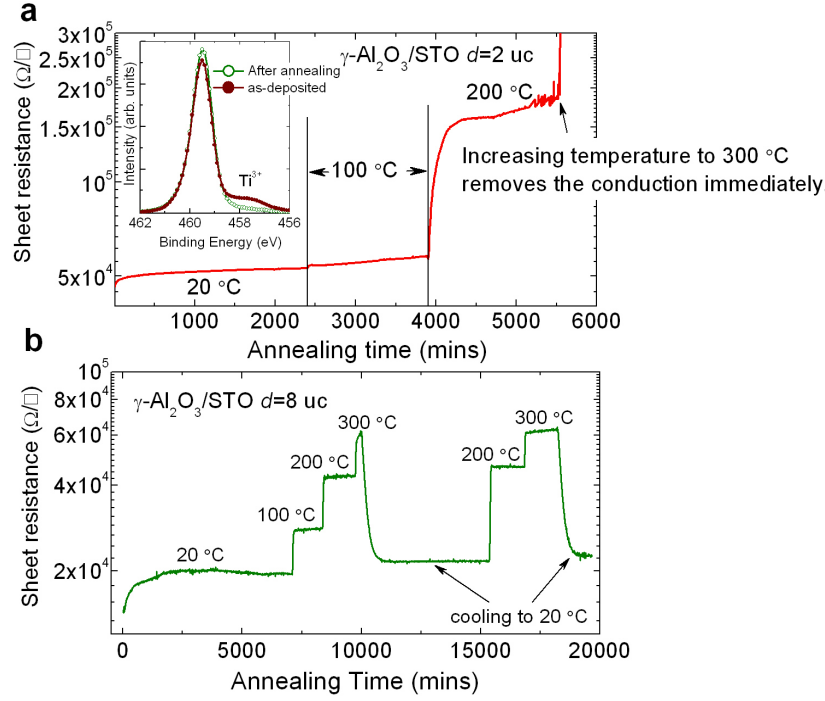
and $g_s=2$, this gives an $n_{2D}=7.1 \times 10^{11} \text{ cm}^{-2}$. As a consequence, the sheet carrier density deduced from

the SdH oscillations show significant discrepancy from that obtained from the Hall measurements. A

similar phenomenon is also found in the 2DEGs at the LAO/STO interface [16, 27] and in δ -doped

STO heterostructures [28, 29, 47]. This is probably due to the existence of low mobility 2D or 3D

subbands which do not satisfy the conditions to exhibit SdH oscillations ($\hbar\omega_c \geq k_B T$ and $\omega_c \tau \geq 1$) but contribute nevertheless to the Hall signal [48]. For $n_{2D} = 7.1 \times 10^{11} \text{ cm}^{-2}$, the corresponding Fermi wavelength $\lambda_F = 2\pi/k_F = \sqrt{2\pi/n}$ is about 30 nm. The mean free path l_{mfp} of these electrons with a $\tau = 4.96 \times 10^{-12} \text{ s}$ and $m^* = 1.22 m_e$ (see the main text) is $l_{\text{mfp}} = v_F \tau = \hbar k_F \tau / m^* = 99 \text{ nm}$ ($v_F = 20000 \text{ m/s}$), which is approximately 10 times larger than the l_{mfp} for LAO/STO interfaces [4, 16].



Supplementary Figure S6. High temperature annealing of the $\gamma\text{-Al}_2\text{O}_3/\text{STO}$ interface in 1 bar pure oxygen. **a**, The annealing of a $\gamma\text{-Al}_2\text{O}_3/\text{STO}$ interface with $d=2$ uc indicates that the 2DEG is almost stable up to 200 °C. However, increasing the annealing temperature up to 300 °C removes the conductivity in several minutes and suppresses the Ti^{3+} signal almost to zero (inset of **a** for the Ti $2p_{3/2}$ XPS spectra before and after annealing). In contrast, as shown in **b**, the $\gamma\text{-Al}_2\text{O}_3/\text{STO}$ interface with a thicker film of $d=8$ uc can survive the annealing at 300 °C for more than 24 hours. Furthermore, the conductivity shows negligible changes after cooling down to room temperature. Considering the fact that the oxygen diffusion is already feasible at temperatures higher than 100 °C [18], both results suggest that the interfacial bonding in the crystalline $\gamma\text{-Al}_2\text{O}_3/\text{STO}$ interface has a stabilization effect on the 2DEG, otherwise the conduction will be removed after such annealing as observed in the amorphous STO-based heterostructures [18]. Moreover, the removal of conductivity after suitable

oxygen annealing strongly suggests that the interfacial conduction is related to oxygen vacancies.

Additionally, for both samples, a slight increase of the sheet resistance is observed at the beginning of the measurement. This may be due to the removal of the contribution from photoconduction.

Supplementary References

41. Terashima, T. *et al.* Reflection high-energy electron diffraction oscillations during epitaxial growth of high-temperature superconducting oxides. *Phys. Rev. Lett.* **65**, 2684-2687 (1990).
42. Dobson, P. J., Joyce, B. A., Neave, J. H. & Zhang, J. Current understanding and applications of the RHEED intensity oscillation technique. *J. Crys. Growth* **81**, 1-8 (1987).
43. Kim, J. S. *et al.* Nonlinear Hall effect and multichannel conduction in LaTiO₃/SrTiO₃ superlattices. *Phys. Rev. B* **82**, 201407(R) (2010).
44. Armijo, J. S. The kinetics and mechanism of solid state spinel formation-a review and critique. *Oxidation of Metals* **1**, 171-198 (1969).
45. Murphy, S. T. Cation diffusion in magnesium aluminate spinel. *Solid State Ionics* **180**, 1-8 (2009).
46. Mizoguchi, T., Takahashi, N., & Lee, H. S. First-principles study on migration mechanism in SrTiO₃. *Appl. Phys. Lett.* **98**, 091909 (2011).
47. Kim, M. *et al.* Fermi surface and superconductivity in low-density high-mobility δ -doped SrTiO₃. *Phys. Rev. Lett.* **107**, 106801 (2011).
48. Khalsa, G. & MacDonald, A. H. Theory of the SrTiO₃ surface state two-dimensional electron gas. arXiv:1205.4362v1 (2012).